Atmos. Chem. Phys. Discuss., https://doi.org/10.5194/acp-2018-443
Manuscript under review for journal Atmos. Chem. Phys.
Discussion started: 15 May 2018

Atmospheric Chemistry and Physics Discussions

Chlorine-initiated oxidation of n-alkanes under high NOx conditions: Insights into secondary organic aerosol composition and volatility using a FIGAERO-CIMS

Dongyu S. Wang and Lea Hildebrandt Ruiz

Department of Chemical Engineering, The University of Texas at Austin, Austin, TX 78756, USA

Correspondence to: Lea Hildebrandt Ruiz (lhr@che.utexas.edu)

Abstract. Chlorine-initiated oxidation of *n*-alkanes (C_{8-12}) under high nitrogen oxides conditions was investigated. Observed secondary organic aerosol yields (0.16 to 1.65) are higher than those for OH-initiated oxidation of C_{8-12} alkanes (0.04 to 0.35). A High-Resolution Time-of-Flight Chemical Ionization Mass Spectrometer coupled to a Filter Inlet for Gases and AEROsols (FIGAERO-CIMS) was used to characterize the gas- and particle-phase molecular composition. Chlorinated organics were observed, which likely originated from chlorine addition to the double bond present on the heterogeneously produced dihydrofurans. A two-dimensional thermogram representation was developed to visualize composition and relative volatility of organic aerosol components using unit-mass resolution data. Evidence of oligomer formation, thermal fragmentation and thermal decomposition was observed. Aerosol yield and oligomer formation were suppressed under humid conditions (35 to 67 % RH) relative to dry conditions (under 5 % RH). The temperature at peak desorption signal, T_{max}, a proxy for aerosol volatility, was shown to change with aerosol filter loading, which should be constrained when evaluating aerosol volatilities using the FIGAERO-CIMS. Results suggest that long-chain anthropogenic alkanes could contribute significantly to ambient aerosol loading over their atmospheric lifetime.

1 Introduction

Alkanes account for up to 90% of all anthropogenic hydrocarbon emissions and 12 % (140 Tg yr^{-1}) of annual non-methane hydrocarbon emissions (Fraser et al., 1997; Goldstein and Galbally, 2007; Guenther et al., 2012; Rogge et al., 1993; Schauer et al., 1999, 2002). Linear, branched, cyclic alkanes, and aromatics are major components of gasoline, diesel, motor oil, and other petroleum products (Caravaggio et al., 2007; Kleeman et al., 2008; Schauer et al., 1999). Depending on its vapor pressure, the alkane can be emitted as volatile organic compound (VOC), intermediate-volatility organic compound (IVOC), semi-volatile organic compound (SVOC), or primary organic aerosol (POA). Evaporation of POA due to dilution can provide additional gas-phase alkanes, which can undergo photooxidation initiated by OH, NO_3, as well as chlorine radicals (Aschmann and Atkinson, 1995; Atkinson and Arey, 2003). Consequently, alkanes can have significant contributions to SOA production in urban environments (Dunmore et al., 2015). Hydrocarbon-like organic aerosol, which is often associated with POA and alkane oxidation, contributes on average 36 % to fine particulate matter (PM_1) in urban environments (Zhang et al., 2007).

Influences of alkane emission and oxidation on SOA formation can be observed in remote regions as well (Carlton et al., 2010; Chrit et al., 2017; Hoyle et al., 2011; Minguillón et al., 2011, 2016; Patokoski et al., 2014; Saito et al., 2004; Sartelet et al., 2012). Alkane emissions can be sporadic and scattered, complicating both monitoring and modeling efforts (Lyon et al., 2015; Zavala-Araiza et al., 2015, 2017). Using laboratory results on OH-initiated SOA formation from alkanes under low- and high-NO_x conditions (Jordan et al., 2008; Lamkaddam et al., 2017; Lim and Ziemann, 2009a, 2005, 2009b; Loza et al., 2014; Presto et al., 2009, 2010; Schilling Fahnestock et al., 2015; Takekawa et al., 2003; Tkacik et al., 2012; Yee et al., 2012, 2013; Zhang et al., 2014), model prediction for OA concentration can be improved, though the predicated OA is often less oxidized than observed (Bahreini et al., 2012; Decarlo et al., 2010; Dzepina et al., 2009; de Gouw et al., 2011; Murphy and Pandis, 2009; Shrivastava et al., 2008; Zhang et al., 2007), which could point to missing oxidants (e.g. chlorine radicals) and SOA oxidation mechanisms in the models (Murphy and Pandis, 2009).

Recent field studies have identified reactive chlorine compounds in diverse locales from natural and anthropogenic sources (Faxon and Allen, 2013; Finlayson-Pitts, 2010; Saiz-Lopez and von Glasow, 2012; Simpson et al., 2015). Tropospheric chlorine chemistry can enhance ozone production (Tanaka et al., 2003). Nighttime production of nitryl chloride mediated by heterogenous uptake of NO_x onto chloride-containing particles represents an ubiquitous source for reactive chlorine (Thornton et al., 2010). In addition to nighttime chemistry, biomass burning could also act as a source of $ClNO_2$ (Ahern et al., 2018). $ClNO_2$ photolysis can dominate RO_2 radical production in the early morning (Riedel et al., 2012). Akin to hydroxyl radicals, chlorine radicals initiate reactions with alkanes via hydrogen-abstraction, forming hydrogen chloride (HCl) and alkylperoxy radicals (RO_2). The biomolecular gas-phase reaction rate constants with linear alkanes for hydroxyl radicals and chlorine radicals increase with the alkane chain length. Consequently, the reaction rate constants for chlorine and linear C_{8-12} alkanes range from 4.05×10^{-10} (octane) to 5.36×10^{-10} cm^{-3} $molecules^{-1}$ s^{-1} (dodecane) at 298 K and 1 atm (Aschmann and Atkinson, 1995), which is over an order of magnitude higher than the rate constants for hydroxyl radicals, 8.11×10^{-12} (octane) to 1.32×10^{-11} cm^{-3} $molecules^{-1}$ s^{-1} (dodecane; Atkinson and Arey, 2003). Studies show that chlorine-initiated oxidation of volatile organic compounds such as isoprene, monoterpenes, toluene, and polycyclic aromatic hydrocarbons can lead to rapid SOA formation with high yields (Cai et al., 2008; Cai and Griffin, 2006; Huang et al., 2014; Karlsson et al., 2001; Ofner et al., 2013; Riva et al., 2015; Wang and Hildebrandt Ruiz, 2017).

Although all initial C_{8-12} alkane-Cl oxidation products are expected be non-chlorinated, formation of alkane-derived organochlorides is possible from chlorine addition to the multi-generational products. Studies show that the oxidation of alkanes with 5 or more linear carbons produces 1,4-hydroxycarbonyl that can undergo a rate-limiting, acid-catalyzed heterogenous reaction to produce dihydrofuran (DHF) compounds (Atkinson et al., 2008; Holt et al., 2005; Jordan et al., 2008; Lim and Ziemann, 2009b, 2009c). DHF is highly reactive: For 2,5-dihydrofuran, the bimolecular reaction rate constants with O_3, OH and Cl are $1.65 \pm 0.31 \times 10^{-17}$, $6.45 \pm 1.69 \times 10^{-11}$, and $4.48 \pm 0.59 \times 10^{-10}$ cm^3 $molecule^{-1}$ s^{-1}, respectively (Alwe et al., 2013, 2014). Chlorine radicals can react with dihydrofuran via both H-abstraction and Cl-addition, producing chlorinated (e.g. dichlorotetrahydrofurans) and non-chlorinated compounds (e.g. furanones) under low NO_x conditions (Alwe et al., 2013). In this study, environmental chamber studies were conducted using long-chain (C_{8-12}) *n*-alkanes and chlorine radicals under high

Atmos. Chem. Phys. Discuss., https://doi.org/10.5194/acp-2018-443
Manuscript under review for journal Atmos. Chem. Phys.
Discussion started: 15 May 2018

NO_x conditions to evaluate the chlorine-initiated SOA formation from alkane and to characterize the molecular composition of gas and aerosol compounds.

2 Methods

2.1 Environmental chamber experiments and instrumentation

Experiments were conducted inside a 10 m^3 Teflon® chamber at 298 K, using UV lights to generate radicals. The NO_2 photolysis rate was measured to characterize the UV intensity (Carter et al., 2005) and was found to be similar to ambient levels (0.53 min^{-1} at 0^o zenith angle) at approximately 0.5 min^{-1}. The chamber relative humidity (RH) ranged from 0 to 67 %. For dry experiments, the chamber was filled with dried clean air supplied by a clean air generator (model 737R, Aadco). For humid experiments (i.e. RH > 20 %), the chamber was flushed overnight with humidified clean air. To reduce wall-loss, dried ammonium sulfate seed particles were injected into the chamber. The seed particles were generated from a 0.01 M aqueous ammonium sulfate solution using an aerosol generation system (AGS 2002, Brechtel). Chlorine gas (101 ppm in N_2, Airgas) was injected as the chlorine radical precursor. Each *n*-alkane (*n*-octane, 99 %; *n*-decane, 99 %; dodecane > 99%, Sigma-Aldrich) was first injected into a glass gas sampling tube (Kimble-Chase, 250 mL), which was flushed with gently heated clean air into the chamber at 2 lpm for at least 30 minutes. Precursor NO (9.98 ppm in N_2, Airgas) and NO_2 (9.86 ppm in N_2, Airgas) were injected into the chamber using a mass flow controller (GFC17, Aalborg). Initial concentrations of VOC and oxidant precursors are summarized in Table 1. Gas-phase NO and NO_2 concentrations were monitored by a chemiluminescence monitor (200E, Teledyne). The O_3 concentration was monitored using a photometric ozone analyzer (400E, Teledyne). The start of photooxidation, initiated by turning on all the UV lights after the precursors were well-mixed in the chamber, was designated as the reference point (i.e. time 0 min) for each experiment. UV lights were turned off after 60 minutes. On the day before and after each SOA formation experiment, ammonium sulfate seed particles and 50 ppb of chlorine gas were injected into the chamber. UV lights were turned on to generate chlorine radicals and remove residual reactive organic compounds in the chamber. Minimal SOA formation was observed during these cleaning experiments.

Particle size distributions were characterized using a scanning electrical mobility system (SEMS, Brechtel model 2002). The particle-phase bulk chemical composition was measured using an aerosol chemical speciation monitor (ACSM, Aerodyne). The ACSM was calibrated with 300nm size-selected ammonium nitrate and ammonium sulfate aerosols generated from nebulized 0.005 M solutions using the AGS to determine the nitrate response factor (RF) and relative ionization efficiencies (RIE) for ammonium and sulfate, which are required for ion-to-mass signal conversions. Using electron impact ionization, the ACSM can measure the submicron, non-refractory aerosol bulk composition at one minute intervals (Budisulistiorini et al., 2013; Ng et al., 2011a). Using a standard fragmentation table (Allan et al., 2004), the ACSM can speciate the aerosol content into organics, nitrate, sulfate, ammonium, and chloride (Ng et al., 2011a). The ability of the ACSM to detect organic chloride using HCl^+ (*m/z* 36) has been demonstrated previously for isoprene-Cl SOA (Wang and Hildebrandt Ruiz, 2017). The default RIE_{Chl} value of 1.3 was used for chloride mass conversion. The Cl^+ (*m/z* 35) ion was excluded from

chlorine quantification as it showed inconsistent response to non-refractory chlorides (e.g. ammonium chloride). ACSM data were analyzed in Igor Pro V6.37 (Wavemetrics, Inc.) using ACSM local v1603 (Aerodyne) and other custom routines. Aerosol concentrations were corrected for depositional particle wall loss (Pathak et al., 2007) but not for organic vapor loss (Huang et al., 2018b; Krechmer et al., 2017; Nah et al., 2017).

2.2 FIGAERO-CIMS

A high-resolution time-of-flight chemical ionization mass spectrometer (CIMS, Aerodyne) was used to measure the gas-phase chemical composition using I^- as the chemical ionization reagent. Humidified UHP N_2 was flushed over a methyl iodide permeation tube and then through a ^{210}Po ionizer into the ion-molecule reaction (IMR) chamber of the CIMS. Theory and operation of the CIMS are described in detail elsewhere (Aljawhary et al., 2013; Bertram et al., 2011; Lee et al., 2014; Wang and Hildebrandt Ruiz, 2017). The CIMS inlet is coupled to a filter inlet for gases and aerosols (FIGAERO), which has been used in a number of studies to investigate the chemical composition and volatility of particle-phase compounds (D'Ambro et al., 2017; Gaston et al., 2016; Huang et al., 2018a; Lee et al., 2016; Lopez-Hilfiker et al., 2014, 2015; Stark et al., 2017; Thompson et al., 2017). The FIGAERO system alternated between two operational modes. In the aerosol collection mode, gas-aerosol mixture was drawn through a PTFE filter (Zefluor® 2.0 μm 24mm, Pall Corp.) at 3 SLPM for 15 to 45 minutes while gas species were sampled and analyzed. In the desorption mode, clean air or UHP N_2 was passed through the filter and heated to 200 °C (measured just above the filter) at a rate of 5 to 10 °C min^{-1} for 40 to 20 minutes, respectively. The filter was then soaked at 200 °C for 20 minutes. The volatilized vapor was sampled by the CIMS, and the desorption signal as a function of temperature can be used to construct a one-dimensional (1-D) thermogram (e.g. Fig. 6a). For a monomeric compound, the desorption signal as a function of temperature is expected to be monomodal (Lopez-Hilfiker et al., 2014). The temperature at the peak desorption signal, T_{max} correlates with the enthalpy of sublimation (dH_{sub}) and the saturation vapor pressure (C^*) of the compound (Lopez-Hilfiker et al., 2014, 2015). However, some compounds may exhibit bimodal or multimodal behavior, with a second desorption mode occurring at much higher temperatures than expected, which is often interpreted as the result of thermal fragmentation or decomposition of larger oligomeric compounds (Huang et al., 2018a; Lopez-Hilfiker et al., 2014; Stark et al., 2017; Wang et al., 2016).

CIMS and FIGAERO data analysis was conducted in Igor Pro with Tofware v2.5.10 (Tofwerk) and custom routines. Hundreds of ions belonging to diverse chemical families can be retrieved from the mass spectra. To simultaneously represent the chemical composition, relative aerosol volatility (i.e. T_{max} distribution), and multimodal thermal desorption behaviors, a two-dimensional (2-D) thermogram framework was developed. The 2-D thermogram is comprised of normalized unit-mass resolution 1-D thermograms, each expressed as a percentage color scale of the maximum desorption signal. The 2-D thermogram development and applications are discussed in detail in Section 3.2.

Atmos. Chem. Phys. Discuss., https://doi.org/10.5194/acp-2018-443
Manuscript under review for journal Atmos. Chem. Phys.
Discussion started: 15 May 2018

3 Results and Discussion

3.1 SOA and organic chloride formation

Experimental conditions and results are summarized in Table 1. Chlorine-alkane SOA yields increased with VOC precursor length, consistent with the trend observed for OH-alkane SOA (Jordan et al., 2008; Lim and Ziemann, 2009b; Presto et al., 2010; Schilling Fahnestock et al., 2015; Yee et al., 2012, 2013). For similarly functionalized alkane oxidation products, the vapor pressure decreases roughly log-linearly as the precursor carbon number increases from 8 to 15 (Jordan et al., 2008; Presto et al., 2010). Comparison of the unit-mass ACSM spectra for octane (Exp. 3), decane (Exp. 7), and dodecane (Exp. 11) SOA in Fig. S1 shows a consistent increase in the fractional contributions to the bulk OA mass (i.e. $f_{m/z}$) by organic ions at *m/z* 27 ($C_2H_3^+$), 41 ($C_3H_5^+$), 55 ($C_4H_7^+$) and 57 ($C_4H_9^+$) with increasing alkane length. Select odd *m/z* ions, noticeably *m/z* 55 and 57, have been used as tracers for hydrocarbon-like organic aerosol (HOA), and sometimes for primary aerosol emissions as well (Ng et al., 2011b; Ulbrich et al., 2009). Given the same oxidation conditions, SOA products derived from longer alkane precursors appeared less oxidized, as seen by the decrease in f_{44} (presumably mostly CO_2^+), but more hydrocarbon-like, as seen by the increase in f_{55}, consistent with previous observations (Lambe et al., 2012; Loza et al., 2014). The results are summarized in Table 1. As the alkane chain length increases, the increased SOA production also favors the partitioning of semi-volatile compounds into the particle-phase (Donahue et al., 2006; Pankow, 1994), further lowering f_{44}.

Time series of gas-phase NO, NO_2, O_3, Cl_2, and suspended particle-phase organics and chlorine concentrations during photooxidation are shown in Fig. 1 using dodecane-Cl oxidation under low RH (Exp. 11) as the representative example. The Cl_2 concentration was estimated using I^- CIMS by tracking the Cl^- ion. The NO concentration decreased sharply at the beginning of the experiment accompanied by rapid ozone production and increases in NO_2 concentration. SOA production was most rapid during this initial period (0 to 10 min). Afterwards, at around 15 min in Fig. 1, the concentrations of NO_2 and ozone stabilized. Oxidation continued under UV driven by chlorine radicals, and the SOA concentration began to decay due to oxidative fragmentation (Kroll et al., 2011; Lambe et al., 2012; Wang and Hildebrandt Ruiz, 2017). The ozone production continued slowly under UV at ~0.24 ppb min^{-1}. Slight NO_2 production (< 0.1 ppb min^{-1}) was also observed, which may be due to production of nitrous acid (HONO) on the Teflon® surface, a common background contaminant in environmental chambers (Carter et al., 2005; Rohrer et al., 2004). Particulate nitrate (NO_3) followed the bulk organics trend and the ratios of NO_3 to organic mass are summarized in Table 1. The NO_3 to organics ratio did not change significantly for different alkane precursors, likely because the gas-phase oxidation chemistry is similar for C_8 to C_{17} alkanes (Jordan et al., 2008). The branching ratio for RO_2 + NO reaction increases only slightly from C_8 (0.24) to C_{12} (0.29), plateauing after C_{13} for OH-initiated oxidations (Arey et al., 2001; Atkinson et al., 1983; Yeh and Ziemann, 2015). The decrease in NO_3 to organics ratio from decane-Cl SOA (0.12-0.13) to dodecane-Cl SOA (0.08-0.11) is consistent with partitioning of more volatile, less oxidized compounds into the particle phase under higher SOA loading conditions. The SOA production was dependent on the initial NO and NO_2 concentrations, as shown in Fig. S2. In all experiments, NO decayed to zero in the first 10 minutes of the experiment, during which time most of the SOA formation occurred. Higher initial NO concentrations led to higher SOA yields and lower ozone

Atmos. Chem. Phys. Discuss., https://doi.org/10.5194/acp-2018-443
Manuscript under review for journal Atmos. Chem. Phys.
Discussion started: 15 May 2018

Atmospheric Chemistry and Physics Discussions

production for all precursors, as shown in Table 1 and Fig. S2. This is similar to alkane-OH SOA formation, where higher NO concentrations lead to more abundant organic nitrate formation, which increases the SOA volume (Schilling Fahnestock et al., 2015) and density (Loza et al., 2014). The alkane-Cl SOA yields, ranging from 0.16 (octane) to 1.65 (dodecane), are 4 times higher than the alkane-OH SOA yields (0.04 for octane and 0.35 for dodecane) that were obtained using 1 ppm alkane, 10 ppm methyl nitrite, and 10 ppm NO (Lim and Ziemann, 2009a), much higher than the precursor concentrations used here (13 to 15 ppb alkanes, < 40 ppb NO_x, 40 ppb Cl_2).

Although the initial chlorine-alkane reactions proceed via a H-abstraction pathway, particulate chlorine was observed using the ACMS as shown in Fig. 1. Direct halogenation of the $C_{8\text{-}12}$ alkyl radicals is expected to be minimal, given the low amounts of Cl_2 present (40 ppb). A carbon-carbon double bond is required to enable chlorine addition reactions and organic chlorine formation. The heterogeneous production of dihydrofuran (DHF) via 1,4-hydroxycarbonyl uptake, acid-catalyzed isomerization, and dehydration reactions (Atkinson et al., 2008; Jordan et al., 2008; Lim and Ziemann, 2009c, 2009b), followed by Cl addition to the DHF double bond, could be the source of observed organic chlorine. A condensed reaction pathway is shown in Fig. 2. The delay in particulate chlorine formation relative to that of bulk organics, as shown in Fig. 1, is consistent with the rate-limiting heterogeneous DHF production (Holt et al., 2005; Zhang et al., 2014). Under high NO_x conditions, the peroxy radical product from the chlorine-addition pathway could react with NO to form a cyclic hemiacetal chloronitrate or an alkoxy radical that would undergo ring-opening reactions. Compounds resembling chloronitrates (e.g. $ONO_2\text{-}C_{12}H_{18}ClO_2{\bullet}I^-$ for dodecane) were tentatively identified in the particle-phase using the FIGAERO but they were not well separated from the shoulder of nearby organonitrate peaks (e.g. $ONO_2\text{-}C_{12}H_{21}O_4{\bullet}I^-$), as shown in Fig. S8. Select $C_{2\text{-}6}$ organochlorides were well-separated from nearby peaks and confirmed by the distinct Cl isotopic signal, the thermograms of which are shown in Fig. S9. The most abundant gas-phase chlorinated organic compounds observed were products of ring-opening reaction pathways such as $C_2H_3ClO_2$ and $C_{4\text{-}6}$ compounds. Small amounts of $C_2H_2Cl_2O_2$ were also observed. Organochloride formation is expected to be lower under humid conditions, where DHF formation is inhibited (Holt et al., 2005; Zhang et al., 2014; Ziemann, 2011). DHF ozonolysis can also compete with chlorination. For instance, under typical marine boundary layer (MBL) conditions, the chlorine-initiated oxidation was estimated to be a significant sink for 2,5-DHF, accounting for 29 % of the reaction in the presence of OH and O_3. In contrast, only 1.8 % of 2,3-DHF consumption was attributed to Cl radical chemistry in the MBL, owing to the increased reactivity of 2,3-DHF (relative to 2,5-DHF) towards ozone and OH radicals (Alwe et al., 2014). The reported alkane-OH reaction mechanisms expects formation of substituted 2,3-DHF (Ziemann, 2011). Although ozone can impose an upper limit on alkane SOA yields and oxidation state, suppressing the multigenerational OH-alkane oxidation chemistry (Zhang et al., 2014), the continued gas-phase processing of OH-alkane and DHF-ozonolysis products via H-abstraction by chlorine radicals could counteract these limitations.

The gas-phase alkane-Cl oxidation products formed under high NO_x conditions were dominated by organonitrates, which was also reflected in the dominance of organonitrates in the particles phase (see Table 1 and Section 3.2). Figure 3 shows the formation of early generation (e.g. hydroxynitrates, $ONO_2\text{-}C_nH_{2n+1}O$) and multi-generational (e.g. oxidized organonitrates, $ONO_2\text{-}C_nH_{2n\text{-}5}O_4$) oxidation products from different alkane precursors. Like the bulk particle phase composition, gas-phase

compounds derived from smaller alkane precursor were more oxidized given similar oxidation conditions (e.g. NO, NO_2, and Cl_2): the signal of oxidation products with similar oxygen numbers (and higher oxidation state) peaked earlier into the photooxidation period for smaller precursors (e.g. ONO_2-$C_8H_{11}O_4$ vs. ONO_2-$C_{12}H_{19}O_4$ in Fig. 3). As oxidation continued, the importance of fragmentation reactions increased relative to that of functionalization reactions (Lambe et al., 2012). Assuming a uniform sensitivity, Figure 4a shows that the gas-phase was dominated by C_3 to C_5 organic nitrates, indicative of fragmentation reactions. The relative abundance of these small, oxidized organic nitrate compounds increased as the VOC precursor length decreased. In addition to hydroxynitrates and hydroxycarbonyl nitrates, dinitrates and trinitrates were also observed. The CIMS was not sensitive towards simple, alkane-derived alkyl nitrates (ONO_2-C_nH_{2n+1}). The lack of sensitivity of the I^- reagent ion towards alkyl and keto nitrates has been reported previously for isoprene and monoterpene-derived organic nitrates (Lee et al., 2016).

3.2 Two-dimensional thermogram

The FIGAERO filter spectra are shown in Fig. 4b for octane (Exp 3), decane (Exp. 7), and dodecane (Exp. 11). A log-scale version of Fig. 4b is shown in Fig. S3. The spectra are calculated from the average desorption ion signals observed when the filter temperature was between 40 and 140 °C, The $C_{8\text{-}12}$ alkane-chlorine SOA share many similarities towards the lower *m/z* (< 320) range which consisted of $C_{\leq 7}$ oxidized organic compounds. For larger alkane precursors, the particle phase composition was dominated by C_n organic nitrates, which are grouped by their degree of oxygenation (i.e. number of non-nitrate O atoms), "O_x", as shown in Fig. 4b. O_1 to O_5 mono-nitrates, O_2 to O_4 dinitrates, and O_1 to O_3 trinitrates dominated each oxygenation group. O_6 to O_8 mono-nitrates were present in the particle-phase but were less abundant than the nearby O_2 to O_4 dinitrates (e.g. $(ONO_2)_2$-$C_{12}H_{20}O_2$ at *m/z* 447 > $(ONO_2)_2$-$C_{12}H_{22}O_2$ at *m/z* 449 > (ONO_2)-$C_{12}H_{17}O_6$ *m/z* 446 > (ONO_2)-$C_{12}H_{19}O_6$ at *m/z* 448). An example of a C_{12} mono-nitrate distribution is shown in Fig. S4. Assuming the same sensitivity towards the different organic nitrates observed, the organic nitrate abundance follows a bell-shaped distribution, similar to field observations for C_5 and C_{10} organic nitrates derived from isoprene and monoterpenes, respectively (Lee et al., 2016). For dodecane mono-nitrates, the abundance peaked around O_3 and O_4 and decreased towards O_2 and O_5, as shown in Fig. S4. Dinitrate abundance decreased from O_2 to O_4. Trinitrate decreased from O_1 to O_3. Similar trends can be observed for octane and decane SOA. Simple hydroxynitrates (e.g. ONO_2-$C_nH_{2n+1}O$) were not observed in the particle phase as they were completely oxidized in the gas-phase, as shown in Fig. 3.

In addition to the identification of aerosol chemical composition, the FIGAERO-CIMS can be used to estimate the aerosol volatility using empirical correlations between C^* and T_{max} (Lopez-Hilfiker et al., 2014, 2015). The particle-phase chemical composition and volatility distribution can be represented in several ways. For instance, desorption signals of select compounds can be normalized against the maximum and plotted on the same 1-D thermogram (ion signal versus filter temperature) to compare their relative volatilities (Lopez-Hilfiker et al., 2014). Scatter plots of oxygen number or O:C ratio versus carbon number colored by T_{max} or particle-phase mass fraction have been used to show changes in aerosol composition (Huang et al., 2018a; Lopez-Hilfiker et al., 2014, 2015). To show the differences of various types of thermal desorption products (i.e.

monomers, thermal fragmentation products, and oligomers), averages of the 1-D thermograms can be shown (Huang et al., 2018a; Lopez-Hilfiker et al., 2015). Scatter plots of T_{max} or the oxidation state of carbon (OS_c) versus molecular weight have been used to distinguish monomers and oligomers for select compounds (Wang et al., 2016). Here we proposed a new framework to represent aerosol composition, relative volatility, and oligomer decomposition simultaneously using 2-D thermograms shown in Fig. 5a-e. As illustrated in Fig. 5a for octane-chlorine SOA, the thermal desorption products could be separated into 5 different groups. Region 1 (m/z < 350, 40 < T_{max} < 90 °C) was composed of low molecular weight semi-volatile organic compounds, including C_1 to C_5 compounds that are not expected to be present in great amounts in the particle-phase. These small organic compounds (detected as I^- adducts) were likely low-temperature thermal fragmentation products. Prominence of ions smaller than m/z 127 (i.e. ions generated not from iodide-adduct formation but possibly acid exchange or charge transfer), including Cl^- and a range of organic ions, was consistent with low-temperature thermal fragmentation. Although I^- is a relatively soft ionization method (compared to electron impact ionization), collision-induced ion fragmentation and cluster dissociation cannot be ruled out as a potential source for non-adducts. Region 2 (350 < m/z < ~700, 40 °C < T_{max} < 120 °C) consisted of monomers, dimers, and some oligomers that showed a positive correlation between T_{max} and molecular weight, which has also been reported for SOA derived from oleic acid (Wang et al., 2016) and from α-pinene (Faxon et al., 2017). In other words, overall, volatility decreased with molecular weight for compounds in region 2. However, within small m/z segments in region 2, the correlation was not strictly linear and the T_{max} varied cyclically. When the carbon and oxygen numbers were fixed (i.e. fixed O:C), the T_{max} decreased (i.e. volatility increased) with increasing H:C (i.e. decreasing OS_c), as shown in Fig. 5e for C_{12} organic nitrates (e.g. ONO_2-$C_{12}H_{19\text{-}25}O_3$ from m/z 400 to 406) observed in dodecane-Cl SOA desorption. Although decreases in OS_c are often associated with increases in the aerosol volatility (Donahue et al., 2011; Kroll et al., 2011), fragmentation notwithstanding, the increase in H:C in each fixed O:C ion group was expected to decrease aerosol volatility. The increase in H:C was likely due to increased hydroxy functionalization over ketone functionalization, which should result in lowering of the saturation vapor pressure according to group contribution theory (Pankow and Asher, 2008). In addition, the T_{max} decreased going from O_3:C_{12} organonitrates (e.g. ONO_2-$C_{12}H_{21}O_3$, T_{max} 95 °C) to O_4:C_{12} organonitrates (e.g. ONO_2-$C_{12}H_{21}O_4$, T_{max} 89 °C). The inconsistencies observed within small m/z segments may be due to loading-dependent T_{max} shift (see Section 3.3), where T_{max} would increase with mass loading. As shown in Fig. 4, the organonitrate ion intensities decreased from O_3 onwards. Overlapping of monomer and oligomer desorption peaks could also increase the apparent T_{max}. Region 3 (T_{max} > 90 °C) consisted of thermal decomposition products across a wide m/z range. Select ions were present in both region 2 and region 3, resulting in bimodal thermal desorption, which can complicate T_{max} estimation using the 2-D thermogram, especially when ions from the two desorption modes show significant overlap. Region 4 (150 °C < T_{max} < 170 °C) consists of mostly thermal decomposition products of the $(NH_4)_2SO_4$ seed particles. There was a clear gap between region 3 and 4. It is possible that the edge of regions 2 and 3 towards high T_{max} range is the FIGAERO-CIMS's volatility detection limit for alkane-Cl SOA, where the energy required for vaporization exceeds that for thermal decomposition (Lopez-Hilfiker et al., 2014). Plateauing of T_{max} towards the high m/z range of region 2 appeared to agree with this hypothesis, where further increases in molecular weight, carbon number, and the degree of oxidation translated to negligible T_{max} increase. Region 5

(*m/z* > 700) likely consisted of high molecular weight, low volatility oligomers. Based on proposed ammonium-catalyzed oligomerization reaction pathways for dodecane-OH SOA under high NO_x conditions, a hemiacetal dimer compound (*m/z* 457) could be produced (Schilling Fahnestock et al., 2015), which would be detected at *m/z* 584 using the I^- FIGAERO. Region 5 therefore likely consisted of $C_{24\text{-}36+}$ (dimers and above) compounds. Thermal desorption of some high molecular weight compounds at temperature much lower than expected (T_{max} ~ 80 °C) was observed for decane SOA and dodecane SOA. No definitive molecular composition was determined for these ions due to low signal intensity and wide range of potential chemical formulas.

The region boundaries can vary depending on the SOA composition as well as mass loading, as will be discussed in Section 3.3. The distribution and general features of the regions are consistent for alkane-Cl SOA formed in different experiments (Fig. 5 and Fig. S7). Comparison of 2-D thermograms for octane-Cl SOA (Fig. 5a) and dodecane- Cl SOA (Fig. 5b) shows that the dodecane SOA contains unique, high molecular weight oligomers (750 < *m/z*), which are accompanied by significantly stronger thermal decomposition features in region 3. Bimodal thermal desorption behavior was observed, as shown in Fig. 5d, which masked the volatility-*m/z* dependence expected for region 2. Compared to SOA formed under dry conditions (Fig 5b, Exp 11), SOA formed under humid conditions (Exp. 12, 67 % RH) contained less high molecular weight oligomers in region 5 and exhibited much less thermal decomposition behavior in region 3, as shown in Fig. 5e, where a more distinct T_{max}-*m/z* correlation could be established as compared to Fig. 5d. RH-induced oligomer suppression has been reported for toluene and α-pinene SOA formation (Hinks et al., 2018; Huang et al., 2018a). The oligomer decrease under high RH could also be due to RH-volatility dependent organic vapor wall loss (Huang et al., 2018b). A clear *m/z* dependence of signal reduction under humid conditions as compared to the dry conditions is shown in Fig. S5. Additionally, SOA yield decreased (37 % for decane and 22 % for dodecane) under humid condition while ozone production increased, which could be related to humidity-induced inhibition of 1,4-hydroxycarbonyl uptake and heterogeneous DHF formation (Holt et al., 2005). DHF is a key intermediate product for multigenerational oxidation chemistry and is reactive towards ozone (Zhang et al., 2014; Ziemann, 2011). Reduction in SOA yields under humid conditions has also been reported for dodecane-OH SOA formation (Schilling Fahnestock et al., 2015). The combined effects of DHF reduction and ozone enhancement would suppress organic chloride formation, which was observed for decane (0-22% reduction relative to bulk organics) and dodecane (22 %) SOA, as shown in Table 1.

3.3 T_{max} shift

As the desorption temperature increased above 140 °C, all dominant ions observed shared the same T_{max}, except for some background ions (e.g. $IHNO_3^-$), as shown in Fig. 5a-c, which were identified to be related to the thermal decomposition of $(NH_4)_2SO_4$ seed particles. From this process, H_2SO_4 vapor molecules produced were either detected as $H_2SO_4 \bullet I^-$ or were deprotonated to produce HSO_4^-, acting as a secondary chemical ionization reagent. Examples of 1st order (e.g. HSO_4^-), 2nd order (e.g. $H_2SO_4 \bullet HSO_4^-$) and 3rd order sulfate (e.g. $(H_2SO_4)_2 \bullet HSO_4^-$) clusters are shown in Fig. S6. It is worth noting that while the T_{max} of sulfate ions was uniform within each filter desorption run, the T_{max} varied between filter runs, which can be

seen in Fig. 5a-c to be between 146 °C and 153 °C. ACSM measurements of suspended sulfate concentrations and the integrated CIMS sulfate desorption signals suggest that the higher T_{max} was associated with higher sulfate filter loadings. Fig. 6a shows the thermograms for $H_2SO_4 \bullet I^-$ and $H_2SO_4 \bullet HSO_4^-$ ions at different filter loadings for pure $(NH_4)_2SO_4$ aerosols, where T_{max} increased from 136 °C to 149 °C as the filter loading increased by 258 %. Using the lowest filter loading tested as the basis for calculating a mass loading ratio (LR_{mass}), it can be shown that the sulfate T_{max} varied linearly with loading in Fig. 6b.

The T_{max} shift phenomena have been observed in several FIGAERO-CIMS studies (D'Ambro et al., 2017; Gaston et al., 2016; Huang et al., 2018a; Lopez-Hilfiker et al., 2015; Thompson et al., 2017). Explanations vary for the observed T_{max} shifts. For example, pinonic acid ($C_{10}H_{16}O_3$) identified in α-Pinene ozonolysis SOA had a much higher T_{max} (40 °C) than expected from calibration (T_{max} < 32 °C), which was attributed to interactions between pinonic acid and other SOA components, causing a decrease in the measured apparent vapor pressure (Lopez-Hilfiker et al., 2015). However, no matrix effects were reported for the pinonic acid T_{max} value (now around 65 °C instead of < 32 °C) obtained from a synthetic mixture of organic acid calibrants (Thompson et al., 2017), where some interactions between different organic molecules might have been expected. Whereas the pure compounds are shown to have sharp monomodal desorption peaks (Lopez-Hilfiker et al., 2014), the field campaign-average thermograms for individual compounds have broader desorption peaks (Thompson et al., 2017), which could be due to the presence of isomers (Thompson et al., 2017), variations in filter loading, differences in aerosol viscosity (Huang et al., 2018a), or interferences from oligomer decomposition products (Lopez-Hilfiker et al., 2014). Another T_{max} shift example was reported for ambient biomass burning measurements, where the levoglucosan T_{max} varied between 58 to 70 °C between 5 pm to 10 am over the course of the campaign (Gaston et al., 2016). Between 10 am to 7 pm, the levoglucosan T_{max} was significantly higher at 100 °C, which was attributed to thermal decomposition of oligomers produced from acid-catalyzed heterogenous reactions, as indicated by the increase in sulfate ion intensities during the same period (Gaston et al., 2016). It was not clear if the sulfate ions measured were derived from sulfuric acid or from the decomposition of $(NH_4)_2SO_4$, which could change the assumption made for aerosol acidity. A T_{max} shift was also observed for isoprene SOA, where the mass and T_{max} of non-nitrated OA decreased with increasing NO_x concentration (D'Ambro et al., 2017). A recent investigation reported increases in T_{max} for α-pinene ozonolysis SOA produced under dry conditions compared to SOA produced under humid conditions (Huang et al., 2018a). A positive correlation between aerosol loading and T_{max} was reported for the first time, and the uniform thermal desorption peak shape assumption was questioned (Huang et al., 2018a). The loading dependence was reported to plateau at around 2 to 4 μg (converted from CIMS ion intensity assuming maximum sensitivity, i.e. that of formic acid). Because increased oligomer content was observed under dry conditions, the authors suggested that viscosity effects were responsible for the observed T_{max} shift (Huang et al., 2018a). It should be noted that plateauing of the T_{max}-loading dependence was demonstrated using averaged values, where ions were lumped based on carbon number. Those that had less than or equal to 10 carbons were designated as monomers, which likely included desorption ions across multiple desorption regions (see Fig. 5). This categorization was perhaps too broad, and the loading dependence of individual ions could be lost after averaging. In contrast, the T_{max} of oligomers, which were defined as compounds that contained more than 10 carbons—thus a more precisely defined group—only began to plateau at higher concentrations.

Atmos. Chem. Phys. Discuss., https://doi.org/10.5194/acp-2018-443
Manuscript under review for journal Atmos. Chem. Phys.
Discussion started: 15 May 2018

Atmospheric Chemistry and Physics Discussions

The T_{max} mass dependence was also observed for alkane-Cl SOA. For Exp.6, three filters were collected and analyzed. The first filter was collected at 3 SLPM for 45 mins, followed by the second filter at 3 SLPM for 30 mins, and afterwards the third filter at 3 SLPM for 15 mins. The ratios of the unit-mass integrated ion signals during the desorption period for the first two filters relative to that of the third filter are shown in Fig. S7a. The associated 2-D thermograms are shown in Fig. S7b-d. Compounds in the T_{max}-*m/z* dependence region (Region 2) showed a 10 to 20 ºC T_{max} increase from the lowest filter loading to the highest filter loading conditions. T_{max} of sulfate-related ions increased from 149 ºC to 172 ºC with filter loading. The increase of enhancement ratio with *m/z*, as shown in Fig. S7a, reflects the changes in the composition of suspended aerosol in the chamber over time. Between the first (high-loading) filter collection and the third (low-loading) filter collection, volatility-dependent vapor wall loss may lead to a disproportionate decrease in high molecular weight, low volatility compounds (Huang et al., 2018b; Krechmer et al., 2016), resulting in increasingly greater enhancement towards the high *m/z* region shown in Fig. S7a. The correlation between T_{max} shift and integrated desorption signal for organics was not linear, unlike for ammonium sulfate, which may be due to matrix or saturation effects as previously suggested (Huang et al., 2018a). Overall, our results show that the T_{max} for organic and inorganic compounds varies with loading, which needs to be accounted for when estimating aerosol component volatility from the empirical correlations between T_{max} and C^* using the FIGAERO-CIMS.

4 Conclusion

Environmental chamber experiments were carried out to investigate the chlorine-initiated oxidation of C_{8-12} linear alkanes under high NO_x conditions. Rapid SOA formation and ozone production were observed. SOA yields increase with precursor length, consistent with alkane-OH SOA formation. Under similar oxidation conditions, alkane-Cl SOA exhibited more hydrocarbon-like characteristics as the alkane precursor length increased, as indicated by the ACSM measurements. This bulk SOA observation is consistent with gas- and particle-phase CIMS measurements, which identified more oxidized reaction products derived from smaller alkane precursors. CIMS measurements also confirmed that organonitrates dominated the gas- and particle-phase composition. Using the ACSM and the FIGAERO-CIMS, trace amounts of alkane-derived organochlorides were observed, produced via chlorine-addition to the heterogeneously produced dihydrofuran compounds. Organochloride and bulk SOA production were suppressed under humid conditions, whereas ozone production increased. Under such conditions, the SOA yields observed for chlorine-initiated oxidation of octane (0.24), decane (0.50), and for dodecane (1.10) were still much higher than those observed for OH-initiated oxidation of the respective alkanes. Overall, these results show that chlorine-alkane oxidation could be an important pathway for SOA production and ageing.

A clear mass loading dependence for T_{max} was demonstrated using ammonium sulfate aerosols and alkane-Cl SOA, indicating that the quantitative assessment of C^* from T_{max} using the FIGAERO-CIMS needs to account for variations in filter loading. A unit-mass-resolution 2-D FIGAERO-CIMS thermogram framework was developed. The 2D thermograms demonstrate a clear relationship between molecular weight and volatility of aerosol components, and RH-induced suppression

of oligomer formation. When used in conjunction with high-resolution ion fitting, the 2D thermogram can be a powerful tool for interpreting the chemical composition and volatility distribution of particle-phase compounds.

Acknowledgements

This material is based upon work supported by the Welch Foundation under Grant No. F-1925 and the National Science Foundation under Grant No. 1653625. We thank P.J. Ziemann and L.B. Algrim for helpful discussions on the formation of organochloride. We thank the Air & Waste Management Association for the Air Quality Research and Study Scholarship.

References

Ahern, A. T., Goldberger, L., Jahl, L., Thornton, J. and Sullivan, R. C.: Production of N2O5 and ClNO2 through Nocturnal Processing of Biomass-Burning Aerosol, Environ. Sci. Technol., 52(2), 550–559, doi:10.1021/acs.est.7b04386, 2018.

Aljawhary, D., Lee, a. K. Y. and Abbatt, J. P. D.: High-resolution chemical ionization mass spectrometry (ToF-CIMS): Application to study SOA composition and processing, Atmos. Meas. Tech., 6(11), 3211–3224, doi:10.5194/amt-6-3211-2013, 2013.

Allan, J. D., Delia, A. E., Coe, H., Bower, K. N., Alfarra, M. R., Jimenez, J. L., Middlebrook, A. M., Drewnick, F., Onasch, T. B., Canagaratna, M. R., Jayne, J. T. and Worsnop, D. R.: A generalised method for the extraction of chemically resolved mass spectra from Aerodyne aerosol mass spectrometer data, J. Aerosol Sci., 35(7), 909–922, doi:10.1016/j.jaerosci.2004.02.007, 2004.

Alwe, H. D., Walawalkar, M., Sharma, A., Pushpa, K. K., Dhanya, S. and Naik, P. D.: Rate coefficients for the gas-phase reactions of chlorine atoms with cyclic ethers at 298 K, Int. J. Chem. Kinet., 45(5), 295–305, doi:10.1002/kin.20765, 2013.

Alwe, H. D., Walavalkar, M. P., Sharma, A., Dhanya, S. and Naik, P. D.: Tropospheric oxidation of cyclic unsaturated ethers in the day-time: Comparison of the reactions with Cl, OH and O3 based on the determination of their rate coefficients at 298K, Atmos. Environ., 82, 113–120, doi:10.1016/j.atmosenv.2013.10.009, 2014.

Arey, J., Aschmann, S. M., Kwok, E. S. C. and Atkinson, R.: Alkyl Nitrate , Hydroxyalkyl Nitrate , and Hydroxycarbonyl Formation from the NOx-Air Photooxidations of C5-C8 n-Alkanes, J. Phys. Chem. A, 105(x), 1020–1027, doi:10.1021/jp003292z, 2001.

Aschmann, S. M. and Atkinson, R.: Rate constants for the gas-phase reactions of alkanes with Cl atoms at 296 ± 2 K, Int. J. Chem. Kinet., 27(6), 613–622, doi:10.1002/kin.550270611, 1995.

Atkinson, R. and Arey, J.: Atmospheric Degradation of Volatile Organic Compounds, Chem. Rev., 103(12), 4605–4638, doi:10.1021/cr0206420, 2003.

Atkinson, R., Carter, W. P. L. and Winer, A. M.: Effects of temperature and pressure on alkyl nitrate yields in the NOx photooxidations of n-pentane and n-heptane, J. Phys. Chem., 87(11), 2012–2018, doi:10.1021/j100234a034, 1983.

Atkinson, R., Arey, J. and Aschmann, S. M.: Atmospheric chemistry of alkanes: Review and recent developments, Atmos.

Environ., 42(23), 5859–5871, doi:10.1016/j.atmosenv.2007.08.040, 2008.

Bahreini, R., Middlebrook, A. M., Brock, C. A., de Gouw, J. A., McKeen, S. A., Williams, L. R., Daumit, K. E., Lambe, A. T., Massoli, P., Canagaratna, M. R., Ahmadov, R., Carrasquillo, A. J., Cross, E. S., Ervens, B., Holloway, J. S., Hunter, J. F., Onasch, T. B., Pollack, I. B., Roberts, J. M., Ryerson, T. B., Warneke, C., Davidovits, P., Worsnop, D. R. and Kroll, J. H.: Mass Spectral Analysis of Organic Aerosol Formed Downwind of the Deepwater Horizon Oil Spill: Field Studies and Laboratory Confirmations, Environ. Sci. Technol., 46(15), 8025–8034, doi:10.1021/es301691k, 2012.

Bertram, T. H., Kimmel, J. R., Crisp, T. A., Ryder, O. S., Yatavelli, R. L. N., Thornton, J. A., Cubison, M. J., Gonin, M. and Worsnop, D. R.: A field-deployable, chemical ionization time-of-flight mass spectrometer, Atmos. Meas. Tech., 4(7), 1471–1479, doi:10.5194/amt-4-1471-2011, 2011.

Budisulistiorini, S. H., Canagaratna, M. R., Croteau, P. L., Marth, W. J., Baumann, K., Edgerton, E. S., Shaw, S. L., Knipping, E. M., Worsnop, D. R., Jayne, J. T., Gold, A. and Surratt, J. D.: Real-time continuous characterization of secondary organic aerosol derived from isoprene epoxydiols in downtown Atlanta, Georgia, using the aerodyne aerosol chemical speciation monitor, Environ. Sci. Technol., 47(11), 5686–5694, doi:10.1021/es400023n, 2013.

Cai, X. and Griffin, R. J.: Secondary aerosol formation from the oxidation of biogenic hydrocarbons by chlorine atoms, J. Geophys. Res. Atmos., 111(14), 1–14, doi:10.1029/2005JD006857, 2006.

Cai, X., Ziemba, L. D. and Griffin, R. J.: Secondary aerosol formation from the oxidation of toluene by chlorine atoms, Atmos. Environ., 42(32), 7348–7359, doi:10.1016/j.atmosenv.2008.07.014, 2008.

Caravaggio, G. A., Charland, J. P., Macdonald, P. and Graham, L.: N-Alkane Profiles of Engine Lubricating Oil and Particulate Matter By Molecular Sieve Extraction, Environ. Sci. Technol., 41(10), 3697–3701, doi:10.1021/es062233h, 2007.

Carlton, A. G., Bhave, P. V, Napelenok, S. L., Edney, E. D., Sarwar, G., Pinder, R. W., Pouliot, G. A. and Houyoux, M.: Model Representation of Secondary Organic Aerosol in CMAQv4.7, Environ. Sci. Technol., 44(22), 8553–8560, doi:10.1021/es100636q, 2010.

Carter, W. P. L., Cocker, D. R., Fitz, D. R., Malkina, I. L., Bumiller, K., Sauer, C. G., Pisano, J. T., Bufalino, C. and Song, C.: A new environmental chamber for evaluation of gas-phase chemical mechanisms and secondary aerosol formation, Atmos. Environ., 39(40), 7768–7788, doi:10.1016/j.atmosenv.2005.08.040, 2005.

Chrit, M., Sartelet, K., Sciare, J., Pey, J., Marchand, N., Couvidat, F., Sellegri, K. and Beekmann, M.: Modelling organic aerosol concentrations and properties during ChArMEx summer campaigns of 2012 and 2013 in the western Mediterranean region, Atmos. Chem. Phys., 17(20), 12509–12531, doi:10.5194/acp-17-12509-2017, 2017.

D'Ambro, E. L., Lee, B. H., Liu, J., Shilling, J. E., Gaston, C. J., Lopez-Hilfiker, F. D., Schobesberger, S., Zaveri, R. A., Mohr, C., Lutz, A., Zhang, Z., Gold, A., Surratt, J. D., Rivera-Rios, J. C., Keutsch, F. N. and Thornton, J. A.: Molecular composition and volatility of isoprene photochemical oxidation secondary organic aerosol under low- and high-NOx conditions, Atmos. Chem. Phys., 17(1), 159–174, doi:10.5194/acp-17-159-2017, 2017.

Decarlo, P. F., Ulbrich, I. M., Crounse, J., De Foy, B., Dunlea, E. J., Aiken, A. C., Knapp, D., Weinheimer, A. J., Campos, T., Wennberg, P. O. and Jimenez, J. L.: Investigation of the sources and processing of organic aerosol over the Central

Mexican Plateau from aircraft measurements during MILAGRO, Atmos. Chem. Phys., 10(12), 5257–5280, doi:10.5194/acp-10-5257-2010, 2010.

Donahue, N. M., Robinson, A. L., Stanier, C. O. and Pandis, S. N.: Coupled partitioning, dilution, and chemical aging of semivolatile organics, Environ. Sci. Technol., 40(8), 2635–2643, doi:10.1021/es052297c, 2006.

Donahue, N. M., Epstein, S. A., Pandis, S. N. and Robinson, A. L.: A two-dimensional volatility basis set: 1. organic-aerosol mixing thermodynamics, Atmos. Chem. Phys., 11(7), 3303–3318, doi:10.5194/acp-11-3303-2011, 2011.

Dunmore, R. E., Hopkins, J. R., Lidster, R. T., Lee, J. D., Evans, M. J., Rickard, a. R., Lewis, a. C. and Hamilton, J. F.: Diesel-related hydrocarbons can dominate gas phase reactive carbon in megacities, Atmos. Chem. Phys., 15(17), 9983–9996, doi:10.5194/acp-15-9983-2015, 2015.

Dzepina, K., Volkamer, R. M., Madronich, S., Tulet, P., Ulbrich, I. M., Zhang, Q., Cappa, C. D., Ziemann, P. J. and Jimenez, J. L.: Evaluation of recently-proposed secondary organic aerosol models for a case study in Mexico City, Atmos. Chem. Phys., 9(15), 5681–5709, doi:10.5194/acp-9-5681-2009, 2009.

Faxon, C., Hammes, J., Pathak, R. K. and Hallquist, M.: Characterization of organic nitrate constituents of secondary organic aerosol (SOA) from nitrate-radical-initiated oxidation of limonene using High-Resolution Chemical Ionization Mass Spectrometry, 6, 1–25, doi:10.5194/acp-2017-584, 2017.

Faxon, C. B. and Allen, D. T.: Chlorine chemistry in urban atmospheres: A review, Environ. Chem., 10(3), 221–233, doi:10.1071/EN13026, 2013.

Finlayson-Pitts, B. J.: Halogens in the troposphere, Anal. Chem., 82(3), 770–776, doi:10.1021/ac901478p, 2010.

Fraser, M. P., Cass, G. R., Simoneit, B. R. T. and Rasmussen, R. A.: Air quality model evaluation data for organics. 4. C2-C36 non- aromatic hydrocarbons, Environ. Sci. Technol., 31(8), 2356–2367, doi:10.1021/es960980g, 1997.

Gaston, C. J., Lopez-Hilfiker, F. D., Whybrew, L. E., Hadley, O., McNair, F., Gao, H., Jaffe, D. A. and Thornton, J. A.: Online molecular characterization of fine particulate matter in Port Angeles, WA: Evidence for a major impact from residential wood smoke, Atmos. Environ., 138, 99–107, doi:10.1016/j.atmosenv.2016.05.013, 2016.

Goldstein, A. H. and Galbally, I. E.: Known and unexplored organic constituents in the earth's atmosphere, Environ. Sci. Technol., 41(5), 1514–1521, doi:10.1021/es072476p, 2007.

de Gouw, J. A., Middlebrook, A. M., Warneke, C., Ahmadov, R., Atlas, E. L., Bahreini, R., Blake, D. R., Brock, C. A., Brioude, J., Fahey, D. W., Fehsenfeld, F. C., Holloway, J. S., Le Henaff, M., Lueb, R. A., McKeen, S. A., Meagher, J. F., Murphy, D. M., Paris, C., Parrish, D. D., Perring, A. E., Pollack, I. B., Ravishankara, A. R., Robinson, A. L., Ryerson, T. B., Schwarz, J. P., Spackman, J. R., Srinivasan, A. and Watts, L. A.: Organic Aerosol Formation Downwind from the Deepwater Horizon Oil Spill, Science (80-.)., 331(6022), 1295–1299, doi:10.1126/science.1200320, 2011.

Guenther, A. B., Jiang, X., Heald, C. L., Sakulyanontvittaya, T., Duhl, T., Emmons, L. K. and Wang, X.: The model of emissions of gases and aerosols from nature version 2.1 (MEGAN2.1): An extended and updated framework for modeling biogenic emissions, Geosci. Model Dev., 5(6), 1471–1492, doi:10.5194/gmd-5-1471-2012, 2012.

Hinks, M. L., Montoya-Aguilera, J., Ellison, L., Lin, P., Laskin, A., Laskin, J., Shiraiwa, M., Dabdub, D. and Nizkorodov, S.

A.: Effect of relative humidity on the composition of secondary organic aerosol from the oxidation of toluene, Atmos. Chem. Phys., 18(3), 1643–1652, doi:10.5194/acp-18-1643-2018, 2018.

Holt, T., Atkinson, R. and Arey, J.: Effect of water vapor concentration on the conversion of a series of 1,4-hydroxycarbonyls to dihydrofurans, J. Photochem. Photobiol. A Chem., 176(1–3 SPEC. ISS.), 231–237, doi:10.1016/j.jphotochem.2005.08.029, 2005.

Hoyle, C. R., Boy, M., Donahue, N. M., Fry, J. L., Glasius, M., Guenther, A., Hallar, A. G., Huff Hartz, K., Petters, M. D., Petäjä, T., Rosenoern, T. and Sullivan, A. P.: A review of the anthropogenic influence on biogenic secondary organic aerosol, Atmos. Chem. Phys., 11(1), 321–343, doi:10.5194/acp-11-321-2011, 2011.

Hu, W., Campuzano-Jost, P., Day, D. A., Croteau, P., Canagaratna, M. R., Jayne, J. T., Worsnop, D. R. and Jimenez, J. L.: Evaluation of the new capture vaporizer for aerosol mass spectrometers (AMS) through field studies of inorganic species, Aerosol Sci. Technol., 51(6), 735–754, doi:10.1080/02786826.2017.1296104, 2017.

Huang, M., Liu, X., Hu, C., Guo, X., Gu, X., Zhao, W., Wang, Z., Fang, L. and Zhang, W.: Aerosol laser time-of-flight mass spectrometer for the on-line measurement of secondary organic aerosol in smog chamber, Meas. J. Int. Meas. Confed., 55(3), 394–401, doi:10.1016/j.measurement.2014.05.038, 2014.

Huang, W., Saathoff, H., Pajunoja, A., Shen, X., Naumann, K.-H., Wagner, R., Virtanen, A., Leisner, T. and Mohr, C.: α-Pinene secondary organic aerosol at low temperature: chemical composition and implications for particle viscosity, Atmos. Chem. Phys., 18(4), 2883–2898, doi:10.5194/acp-18-2883-2018, 2018a.

Huang, Y., Zhao, R., Charan, S. M., Kenseth, C. M., Zhang, X. and Seinfeld, J. H.: Unified Theory of Vapor-Wall Mass Transport in Teflon-Walled Environmental Chambers, Environ. Sci. Technol., acs.est.7b05575, doi:10.1021/acs.est.7b05575, 2018b.

Jordan, C. E., Ziemann, P. J., Griffin, R. J., Lim, Y. B., Atkinson, R. and Arey, J.: Modeling SOA formation from OH reactions with C8-C17 n-alkanes, Atmos. Environ., 42(34), 8015–8026, doi:10.1016/j.atmosenv.2008.06.017, 2008.

Karlsson, R. S., Szente, J. J., Ball, J. C. and Maricq, M. M.: Homogeneous aerosol formation by the chlorine atom initiated oxidation of toluene, J. Phys. Chem. A, 105(1), 82–96, doi:10.1021/jp001831u, 2001.

Kleeman, M. J., Riddle, S. G., Robert, M. a. and Jakober, C. a.: Lubricating oil and fuel contributions to particulate matter emissions from light-duty gasoline and heavy-duty diesel vehicles., Environ. Sci. Technol., 42(1), 235–42, doi:10.1021/es071054c, 2008.

Krechmer, J. E., Pagonis, D., Ziemann, P. J. and Jimenez, J. L. L.: Quantification of gas-wall partitioning in Teflon environmental chambers using rapid bursts of low-volatility oxidized species generated in-situ, Environ. Sci. Technol., acs.est.6b00606, doi:10.1021/acs.est.6b00606, 2016.

Krechmer, J. E., Day, D. A., Ziemann, P. J. and Jimenez, J. L.: Direct Measurements of Gas/Particle Partitioning and Mass Accommodation Coefficients in Environmental Chambers, Environ. Sci. Technol., 51(20), 11867–11875, doi:10.1021/acs.est.7b02144, 2017.

Kroll, J. H., Donahue, N. M., Jimenez, J. L., Kessler, S. H., Canagaratna, M. R., Wilson, K. R., Altieri, K. E., Mazzoleni, L.

R., Wozniak, A. S., Bluhm, H., Mysak, E. R., Smith, J. D., Kolb, C. E. and Worsnop, D. R.: Carbon oxidation state as a metric for describing the chemistry of atmospheric organic aerosol., Nat. Chem., 3(2), 133–139, doi:10.1038/nchem.948, 2011.

Lambe, A. T., Onasch, T. B., Croasdale, D. R., Wright, J. P., Martin, A. T., Franklin, J. P., Massoli, P., Kroll, J. H., Canagaratna, M. R., Brune, W. H., Worsnop, D. R. and Davidovits, P.: Transitions from functionalization to fragmentation reactions of laboratory Secondary Organic Aerosol (SOA) generated from the OH oxidation of alkane precursors, Environ. Sci. Technol., 46(10), 5430–5437, doi:10.1021/es300274t, 2012.

Lamkaddam, H., Gratien, A., Pangui, E., Cazaunau, M., Picquet-Varrault, B. and Doussin, J. F.: High-NOxPhotooxidation of n-Dodecane: Temperature Dependence of SOA Formation, Environ. Sci. Technol., 51(1), 192–201, doi:10.1021/acs.est.6b03821, 2017.

Lee, B. H., Lopez-Hilfiker, F. D., Mohr, C., Kurtén, T., Worsnop, D. R. and Thornton, J. A.: An iodide-adduct high-resolution time-of-flight chemical-ionization mass spectrometer: Application to atmospheric inorganic and organic compounds, Environ. Sci. Technol., 48(11), 6309–6317, doi:10.1021/es500362a, 2014.

Lee, B. H., Mohr, C., Lopez-Hilfiker, F. D., Lutz, A., Hallquist, M., Lee, L., Romer, P., Cohen, R. C., Iyer, S., Kurtén, T., Hu, W., Day, D. A., Campuzano-Jost, P., Jimenez, J. L., Xu, L., Ng, N. L., Guo, H., Weber, R. J., Wild, R. J., Brown, S. S., Koss, A., de Gouw, J., Olson, K., Goldstein, A. H., Seco, R., Kim, S., McAvey, K., Shepson, P. B., Starn, T., Baumann, K., Edgerton, E. S., Liu, J., Shilling, J. E., Miller, D. O., Brune, W., Schobesberger, S., D'Ambro, E. L. and Thornton, J. A.: Highly functionalized organic nitrates in the southeast United States: Contribution to secondary organic aerosol and reactive nitrogen budgets, Proc. Natl. Acad. Sci., 113(6), 201508108, doi:10.1073/pnas.1508108113, 2016.

Lim, Y. B. and Ziemann, P. J.: Effects of molecular structure on aerosol yields from OH radical-initiated reactions of linear, branched, and cyclic alkanes in the presence of NOx, Environ. Sci. Technol., 43(7), 2328–2334, doi:10.1021/es803389s, 2009a.

Lim, Y. Bin and Ziemann, P. J.: Products and mechanism of secondary organic aerosol formation from reactions of n-alkanes with OH radicals in the presence of NO x, Environ. Sci. Technol., 39(23), 9229–9236, doi:10.1021/es051447g, 2005.

Lim, Y. Bin and Ziemann, P. J.: Chemistry of Secondary Organic Aerosol Formation from OH Radical-Initiated Reactions of Linear, Branched, and Cyclic Alkanes in the Presence of NO x, Aerosol Sci. Technol., 43(6), 604–619, doi:10.1080/02786820902802567, 2009b.

Lim, Y. Bin and Ziemann, P. J.: Kinetics of the heterogeneous conversion of 1,4-hydroxycarbonyls to cyclic hemiacetals and dihydrofurans on organic aerosol particles, Phys. Chem. Chem. Phys., 11(36), 8029, doi:10.1039/b904333k, 2009c.

Lopez-Hilfiker, F. D., Mohr, C., Ehn, M., Rubach, F., Kleist, E., Wildt, J., Mentel, T. F., Lutz, A., Hallquist, M., Worsnop, D. and Thornton, J. A.: A novel method for online analysis of gas and particle composition: Description and evaluation of a filter inlet for gases and AEROsols (FIGAERO), Atmos. Meas. Tech., 7(4), 983–1001, doi:10.5194/amt-7-983-2014, 2014.

Lopez-Hilfiker, F. D., Mohr, C., Ehn, M., Rubach, F., Kleist, E., Wildt, J., Mentel, T. F., Carrasquillo, a. J., Daumit, K. E.,

Hunter, J. F., Kroll, J. H., Worsnop, D. R. and Thornton, J. a.: Phase partitioning and volatility of secondary organic aerosol components formed from α-pinene ozonolysis and OH oxidation: the importance of accretion products and other low volatility compounds, Atmos. Chem. Phys., 15(14), 7765–7776, doi:10.5194/acp-15-7765-2015, 2015.

Loza, C. L., Craven, J. S., Yee, L. D., Coggon, M. M., Schwantes, R. H., Shiraiwa, M., Zhang, X., Schilling, K. A., Ng, N. L., Canagaratna, M. R., Ziemann, P. J., Flagan, R. C. and Seinfeld, J. H.: Secondary organic aerosol yields of 12-carbon alkanes, Atmos. Chem. Phys., 14(3), 1423–1439, doi:10.5194/acp-14-1423-2014, 2014.

Lyon, D. R., Zavala-Araiza, D., Alvarez, R. A., Harriss, R., Palacios, V., Lan, X., Talbot, R., Lavoie, T., Shepson, P., Yacovitch, T. I., Herndon, S. C., Marchese, A. J., Zimmerle, D., Robinson, A. L. and Hamburg, S. P.: Constructing a Spatially Resolved Methane Emission Inventory for the Barnett Shale Region, Environ. Sci. Technol., 49(13), 8147–8157, doi:10.1021/es506359c, 2015.

Minguillón, M. C., Perron, N., Querol, X., Szidat, S., Fahrni, S. M., Alastuey, A., Jimenez, J. L., Mohr, C., Ortega, A. M., Day, D. A., Lanz, V. A., Wacker, L., Reche, C., Cusack, M., Amato, F., Kiss, G., Hoffer, A., Decesari, S., Moretti, F., Hillamo, R., Teinilä, K., Seco, R., Peñuelas, J., Metzger, A., Schallhart, S., Müller, M., Hansel, A., Burkhart, J. F., Baltensperger, U. and Prévót, A. S. H.: Fossil versus contemporary sources of fine elemental and organic carbonaceous particulate matter during the DAURE campaign in Northeast Spain, Atmos. Chem. Phys., 11(23), 12067–12084, doi:10.5194/acp-11-12067-2011, 2011.

Minguillón, M. C., Pérez, N., Marchand, N., Bertrand, A., Temime-Roussel, B., Agrios, K., Szidat, S., van Drooge, B., Sylvestre, A., Alastuey, A., Reche, C., Ripoll, A., Marco, E., Grimalt, J. O. and Querol, X.: Secondary organic aerosol origin in an urban environment: influence of biogenic and fuel combustion precursors, Faraday Discuss., 189, 337–359, doi:10.1039/C5FD00182J, 2016.

Murphy, B. N. and Pandis, S. N.: Simulating the Formation of Semivolatile Primary and Secondary Organic Aerosol in a Regional Chemical Transport Model, Environ. Sci. Technol., 43(13), 4722–4728, doi:10.1021/es803168a, 2009.

Nah, T., McVay, R. C., Pierce, J. R., Seinfeld, J. H. and Ng, N. L.: Constraining uncertainties in particle-wall deposition correction during SOA formation in chamber experiments, Atmos. Chem. Phys., 17(3), 2297–2310, doi:10.5194/acp-17-2297-2017, 2017.

Ng, N. L., Herndon, S. C., Trimborn, a., Canagaratna, M. R., Croteau, P. L., Onasch, T. B., Sueper, D., Worsnop, D. R., Zhang, Q., Sun, Y. L. and Jayne, J. T.: An Aerosol Chemical Speciation Monitor (ACSM) for Routine Monitoring of the Composition and Mass Concentrations of Ambient Aerosol, Aerosol Sci. Technol., 45(7), 780–794, doi:10.1080/02786826.2011.560211, 2011a.

Ng, N. L., Canagaratna, M. R., Jimenez, J. L., Zhang, Q., Ulbrich, I. M. and Worsnop, D. R.: Real-time methods for estimating organic component mass concentrations from aerosol mass spectrometer data, Environ. Sci. Technol., 45(3), 910–916, doi:10.1021/es102951k, 2011b.

Ofner, J., Kamilli, K. A., Held, A., Lendl, B. and Zetzsch, C.: Halogen-induced organic aerosol (XOA): a study on ultra-fine particle formation and time-resolved chemical characterization, Faraday Discuss., 165, 115–135,

doi:10.1039/c3fd00093a, 2013.

Pankow, J. F.: An absorption model of gas/particle partitioning of organic compounds in the atmosphere, Atmos. Environ., 28(2), 185–188, doi:10.1016/1352-2310(94)90093-0, 1994.

Pankow, J. F. and Asher, W. E.: SIMPOL.1: a simple group contribution method for predicting vapor pressures and enthalpies of vaporization of multifunctional organic compounds, Atmos. Chem. Phys., 8(4), 2773–2796, doi:10.5194/acpd-7-11839-2007, 2008.

Pathak, R. K., Presto, A. A., Lane, T. E., Stanier, C. O., Donahue, N. M. and Pandis, S. N.: Ozonolysis of α-pinene: parameterization of secondary organic aerosol mass fraction, Atmos. Chem. Phys., 7(14), 3811–3821, doi:10.5194/acp-7-3811-2007, 2007.

Patokoski, J., Ruuskanen, T. M., Hellén, H., Taipale, R., Grönholm, T., Kajos, M. K., Petäjä, T., Hakola, H., Kulmala, M. and Rinne, J.: Winter to spring transition and diurnal variation of VOCs in Finland at an urban background site and a rural site, Boreal Environ. Res., 19(2), 79–103, 2014.

Presto, A. A., Miracolo, M. A., Kroll, J. H., Worsnop, D. R., Robinson, A. L. and Donahue, N. M.: Intermediate-volatility organic compounds: A potential source of ambient oxidized organic aerosol, Environ. Sci. Technol., 43(13), 4744–4749, doi:10.1021/es803219q, 2009.

Presto, A. A., Miracolo, M. A., Donahue, N. M. and Robinson, A. L.: Secondary organic aerosol formation from high-NOx Photo-oxidation of low volatility precursors: N-alkanes, Environ. Sci. Technol., 44(6), 2029–2034, doi:10.1021/es903712r, 2010.

Riedel, T. P., Bertram, T. H., Crisp, T. A., Williams, E. J., Lerner, B. M., Vlasenko, A., Li, S. M., Gilman, J., De Gouw, J., Bon, D. M., Wagner, N. L., Brown, S. S. and Thornton, J. A.: Nitryl chloride and molecular chlorine in the coastal marine boundary layer, Environ. Sci. Technol., 46(19), 10463–10470, doi:10.1021/es204632r, 2012.

Riva, M., Healy, R. M., Flaud, P. M., Perraudin, E., Wenger, J. C. and Villenave, E.: Gas- and Particle-Phase Products from the Chlorine-Initiated Oxidation of Polycyclic Aromatic Hydrocarbons, J. Phys. Chem. A, 119(45), 11170–11181, doi:10.1021/acs.jpca.5b04610, 2015.

Rogge, W. F., Hildemann, L. M., Mazurek, M. A., Cass, G. R. and Simoneit, B. R. T.: Sources of Fine Organic Aerosol. 3. Road Dust, Tire Debris, and Organometallic Brake Lining Dust: Roads as Sources and Sinks, Environ. Sci. Technol., 27(9), 1892–1904, doi:10.1021/es00046a019, 1993.

Rohrer, F., Bohn, B., Brauers, T., Brüning, D., Johnen, F.-J., Wahner, a. and Kleffmann, J.: Characterisation of the photolytic HONO-source in the atmosphere simulation chamber SAPHIR, Atmos. Chem. Phys. Discuss., 4(6), 7881–7915, doi:10.5194/acpd-4-7881-2004, 2004.

Saito, T., Kawamura, K., Nakatsuka, T. and Huebert, B. J.: In situ measurements of butane and pentane isomers over the subtropical North Pacific, Geochem. J., 38(5), 397–404, doi:10.2343/geochemj.38.397, 2004.

Saiz-Lopez, A. and von Glasow, R.: Reactive halogen chemistry in the troposphere, Chem. Soc. Rev., 41(19), 6448, doi:10.1039/c2cs35208g, 2012.

Sartelet, K. N., Couvidat, F., Seigneur, C. and Roustan, Y.: Impact of biogenic emissions on air quality over Europe and North America, Atmos. Environ., 53, 131–141, doi:10.1016/j.atmosenv.2011.10.046, 2012.

Schauer, J. J., Kleeman, M. J., Cass, G. R. and Simoneit, B. R. T.: Measurement of emissions from air pollution sources. 2. C1 through C30 organic compounds from medium duty diesel trucks, Environ. Sci. Technol., 33(10), 1578–1587, doi:10.1021/es980081n, 1999.

Schauer, J. J., Kleeman, M. J., Cass, G. R. and Simoneit, B. R. T.: Measurement of emissions from air pollution sources. 5. C1 - C32 organic compounds from gasoline-powered motor vehicles, Environ. Sci. Technol., 36(6), 1169–1180, doi:10.1021/es0108077, 2002.

Schilling Fahnestock, K. A., Yee, L. D., Loza, C. L., Coggon, M. M., Schwantes, R., Zhang, X., Dalleska, N. F. and Seinfeld, J. H.: Secondary Organic Aerosol Composition from C_{12} Alkanes, J. Phys. Chem. A, 119(19), 4281–4297, doi:10.1021/jp501779w, 2015.

Shrivastava, M. K., Lane, T. E., Donahue, N. M., Pandis, S. N. and Robinson, A. L.: Effects of gas particle partitioning and aging of primary emissions on urban and regional organic aerosol concentrations, J. Geophys. Res. Atmos., 113(18), 1–16, doi:10.1029/2007JD009735, 2008.

Simpson, W. R., Brown, S. S., Saiz-Lopez, A., Thornton, J. A. and Von Glasow, R.: Tropospheric Halogen Chemistry: Sources, Cycling, and Impacts, Chem. Rev., 115(10), 4035–4062, doi:10.1021/cr5006638, 2015.

Stark, H., Yatavelli, R. L. N., Thompson, S. L., Kang, H., Krechmer, J. E., Kimmel, J. R., Palm, B. B., Hu, W., Hayes, P. L., Day, D. A., Campuzano-Jost, P., Canagaratna, M. R., Jayne, J. T., Worsnop, D. R. and Jimenez, J. L.: Impact of Thermal Decomposition on Thermal Desorption Instruments: Advantage of Thermogram Analysis for Quantifying Volatility Distributions of Organic Species, Environ. Sci. Technol., 51(15), 8491–8500, doi:10.1021/acs.est.7b00160, 2017.

Takekawa, H., Minoura, H. and Yamazaki, S.: Temperature dependence of secondary organic aerosol formation by photo-oxidation of hydrocarbons, Atmos. Environ., 37(24), 3413–3424, doi:10.1016/S1352-2310(03)00359-5, 2003.

Tanaka, P. L., Riemer, D. D., Chang, S., Yarwood, G., McDonald-Buller, E. C., Apel, E. C., Orlando, J. J., Silva, P. J., Jimenez, J. L., Canagaratna, M. R., Neece, J. D., Mullins, C. B. and Allen, D. T.: Direct evidence for chlorine-enhanced urban ozone formation in Houston, Texas, Atmos. Environ., 37(9–10), 1393–1400, doi:10.1016/S1352-2310(02)01007-5, 2003.

Thompson, S. L., Yatavelli, R. L. N., Stark, H., Kimmel, J. R., Krechmer, J. E., Day, D. A., Hu, W., Isaacman-VanWertz, G., Yee, L., Goldstein, A. H., Khan, M. A. H., Holzinger, R., Kreisberg, N., Lopez-Hilfiker, F. D., Mohr, C., Thornton, J. A., Jayne, J. T., Canagaratna, M., Worsnop, D. R. and Jimenez, J. L.: Field intercomparison of the gas/particle partitioning of oxygenated organics during the Southern Oxidant and Aerosol Study (SOAS) in 2013, Aerosol Sci. Technol., 51(1), 30–56, doi:10.1080/02786826.2016.1254719, 2017.

Thornton, J. A., Kercher, J. P., Riedel, T. P., Wagner, N. L., Cozic, J., Holloway, J. S., Dubé, W. P., Wolfe, G. M., Quinn, P. K., Middlebrook, A. M., Alexander, B. and Brown, S. S.: A large atomic chlorine source inferred from mid-continental reactive nitrogen chemistry., Nature, 464(7286), 271–4, doi:10.1038/nature08905, 2010.

Tkacik, D. S., Presto, A. A., Donahue, N. M. and Robinson, A. L.: Secondary organic aerosol formation from intermediate-

volatility organic compounds: Cyclic, linear, and branched alkanes, Environ. Sci. Technol., 46(16), 8773–8781, doi:10.1021/es301112c, 2012.

Ulbrich, I. M., Canagaratna, M. R., Zhang, Q., Worsnop, D. R. and Jimenez, J. L.: Interpretation of Organic Components from Positive Matrix Factorization of Aerosol Mass Spectrometric Data., Atmos. Chem. Phys., 9, 2891, doi:10.5194/acp-9-2891-2009, 2009.

Wang, D. S. and Hildebrandt Ruiz, L.: Secondary organic aerosol from chlorine-initiated oxidation of isoprene, Atmos. Chem. Phys., 17(22), 13491–13508, doi:10.5194/acp-17-13491-2017, 2017.

Wang, M., Yao, L., Zheng, J., Wang, X., Chen, J., Yang, X., Worsnop, D. R., Donahue, N. M. and Wang, L.: Reactions of Atmospheric Particulate Stabilized Criegee Intermediates Lead to High-Molecular-Weight Aerosol Components, Environ. Sci. Technol., 50(11), 5702–5710, doi:10.1021/acs.est.6b02114, 2016.

Yee, L. D., Craven, J. S., Loza, C. L., Schilling, K. A., Ng, N. L., Canagaratna, M. R., Ziemann, P. J., Flagan, R. C. and Seinfeld, J. H.: Secondary Organic Aerosol Formation from Low-NO_x Photooxidation of Dodecane: Evolution of Multigeneration Gas-Phase Chemistry and Aerosol Composition, J. Phys. Chem. A, 116(24), 6211–6230, doi:10.1021/jp211531h, 2012.

Yee, L. D., Craven, J. S., Loza, C. L., Schilling, K. A., Ng, N. L., Canagaratna, M. R., Ziemann, P. J., Flagan, R. C. and Seinfeld, J. H.: Effect of chemical structure on secondary organic aerosol formation from C12 alkanes, Atmos. Chem. Phys., 13(21), 11121–11140, doi:10.5194/acp-13-11121-2013, 2013.

Yeh, G. K. and Ziemann, P. J.: Gas-Wall Partitioning of Oxygenated Organic Compounds: Measurements, Structure-Activity Relationships, and Correlation with Gas Chromatographic Retention Factor, Aerosol Sci. Technol., 6826(October), 00–00, doi:10.1080/02786826.2015.1068427, 2015.

Zavala-Araiza, D., Lyon, D. R., Alvarez, R. A., Davis, K. J., Harriss, R., Herndon, S. C., Karion, A., Kort, E. A., Lamb, B. K., Lan, X., Marchese, A. J., Pacala, S. W., Robinson, A. L., Shepson, P. B., Sweeney, C., Talbot, R., Townsend-Small, A., Yacovitch, T. I., Zimmerle, D. J. and Hamburg, S. P.: Reconciling divergent estimates of oil and gas methane emissions, Proc. Natl. Acad. Sci., 112(51), 201522126, doi:10.1073/pnas.1522126112, 2015.

Zavala-Araiza, D., Alvarez, R. A., Lyon, D. R., Allen, D. T., Marchese, A. J., Zimmerle, D. J. and Hamburg, S. P.: Super-emitters in natural gas infrastructure are caused by abnormal process conditions, Nat. Commun., 8, 14012, doi:10.1038/ncomms14012, 2017.

Zhang, Q., Jimenez, J. L., Canagaratna, M. R., Allan, J. D., Coe, H., Ulbrich, I., Alfarra, M. R., Takami, A., Middlebrook, A. M., Sun, Y. L., Dzepina, K., Dunlea, E., Docherty, K., DeCarlo, P. F., Salcedo, D., Onasch, T., Jayne, J. T., Miyoshi, T., Shimono, A., Hatakeyama, S., Takegawa, N., Kondo, Y., Schneider, J., Drewnick, F., Borrmann, S., Weimer, S., Demerjian, K., Williams, P., Bower, K., Bahreini, R., Cottrell, L., Griffin, R. J., Rautiainen, J., Sun, J. Y., Zhang, Y. M. and Worsnop, D. R.: Ubiquity and dominance of oxygenated species in organic aerosols in anthropogenically-influenced Northern Hemisphere midlatitudes, Geophys. Res. Lett., 34(13), doi:10.1029/2007GL029979, 2007.

Zhang, X., Schwantes, R. H., Coggon, M. M., Loza, C. L., Schilling, K. A., Flagan, R. C. and Seinfeld, J. H.: Role of ozone

in SOA formation from alkane photooxidation, Atmos. Chem. Phys., 14(3), 1733–1753, doi:10.5194/acp-14-1733-2014, 2014.

Ziemann, P. J.: Effects of molecular structure on the chemistry of aerosol formation from the OH-radical-initiated oxidation of alkanes and alkenes, Int. Rev. Phys. Chem., 30(2), 161–195, doi:10.1080/0144235X.2010.550728, 2011.

5

Atmos. Chem. Phys. Discuss., https://doi.org/10.5194/acp-2018-443
Manuscript under review for journal Atmos. Chem. Phys.
Discussion started: 15 May 2018

Atmospheric Chemistry and Physics Discussions

Table and Figures

Table 1. Summary of Experimental Conditions and Results

Exp #	VOC	NO[a]	NO_2[a]	Cl_2[a]	RH	SOA	Y_{SOA}[b]	f_{44}[c]	f_{55}[d]	f_{NO3}[e]	f_{HCl+}[f]	O_3[g]
1	Octane	35	2	40	5 >	19.5	0.28	1.1 E^{-1}	3.1 E^{-2}	1.3 E^{-1}	1.1 to 1.3 E^{-2}	56
2	Octane	1	36	40	5 >	11.0	0.16	1.0 E^{-1}	2.8 E^{-2}	1.1 E^{-1}	0.7 to 1.1 E^{-2}	69
3	Octane	17	19	40	5 >	16.6	0.24	1.5 E^{-1}	2.4 E^{-2}	1.2 E^{-1}	0.8 to 1.0 E^{-2}	56
4	Octane	17	19	40	35	16.8	0.24	1.0 E^{-1}	3.0 E^{-2}	1.3 E^{-1}	1.1 to 1.4 E^{-2}	60
5	Decane	32	0	40	5 >	68.3	0.84	1.0 E^{-1}	3.2 E^{-2}	1.3 E^{-1}	0.7 to 1.1 E^{-2}	53
6	Decane	0	34	40	5 >	43.1	0.45	7.3 E^{-2}	3.4 E^{-2}	1.3 E^{-1}	0.9 to 1.0 E^{-2}	61
7	Decane	19	18	40	5 >	64.7	0.80	1.3 E^{-1}	3.2 E^{-2}	1.2 E^{-1}	0.9 to 1.2 E^{-2}	51
8	Decane	19	17	40	40	40.7	0.50	8.2 E^{-2}	3.6 E^{-2}	1.2 E^{-1}	0.7 to 1.2 E^{-2}	57
9	Dodecane	35	1	40	5 >	148.6	1.65	2.1 E^{-1}	2.9 E^{-2}	0.8 E^{-1}	0.6 to 0.8 E^{-2}	42
10	Dodecane	0	34	40	5 >	112.8	1.25	6.3 E^{-2}	4.9 E^{-2}	1.0 E^{-1}	0.8 to 1.4 E^{-2}	54
11	Dodecane	17	18	40	5 >	126.4	1.40	6.8 E^{-2}	4.7 E^{-2}	1.1 E^{-1}	0.9 to 1.4 E^{-2}	46
12	Dodecane	20	17	40	67	98.8	1.10	7.2 E^{-2}	4.9 E^{-2}	0.9 E^{-1}	0.7 to 1.1 E^{-2}	62

NO, NO_2, O_3, and Cl_2 concentrations are in ppb. RH is in %. SOA concentration is in μg m^{-3}. Y_{SOA}, f_{44}, f_{44}, f_{NO3}, and f_{Cl} are dimensionless

(a) Initial concentrations

(b) Y_{SOA} is calculated using the maximum SOA concentration and the initial precursor concentrations, which were 70 (octane), 81 (Decane), and 90 (Dodecane) μg m^{-3}, assuming complete VOC consumption

(c) Mass ratio of organic ion fragments at *m/z* 44 (presumably mostly CO_2^+) to the sum of all organic ion fragments observed at peak SOA concentration. Used as a proxy for the SOA extent of oxidation

(d) Mass ratio of organic ion fragments at *m/z* 55 (presumably $C_4H_7^+$) to the sum of all organic ion fragments observed at peak SOA concentration. Used as a proxy for hydrocarbon-like organic aerosol

(e) Mass ratio of the NO_3 ion fragments (i.e. from -ONO_2 functional group) to the organics ion fragments (bulk organics concentration)

(f) Ratio of particulate chlorine mass (estimated using HCl^+ ion fragments in the ACSM) to bulk organics concentration. Lower value is the ratio observed at bulk organics peak and the higher value is the ratio observed at the particulate chlorine peak. Particulate chlorine and bulk organics peak at different times due to the rate-limiting heterogeneous production of dihydrofurans. Chloride concentrations were near detection limits for octane experiments and may be more sensitive towards vaporizer interference effects (Wang and Hildebrandt Ruiz, 2017)(Hu et al., 2017)

(g) The amount of ozone observed when peak SOA concentration was observed

Atmos. Chem. Phys. Discuss., https://doi.org/10.5194/acp-2018-443
Manuscript under review for journal Atmos. Chem. Phys.
Discussion started: 15 May 2018

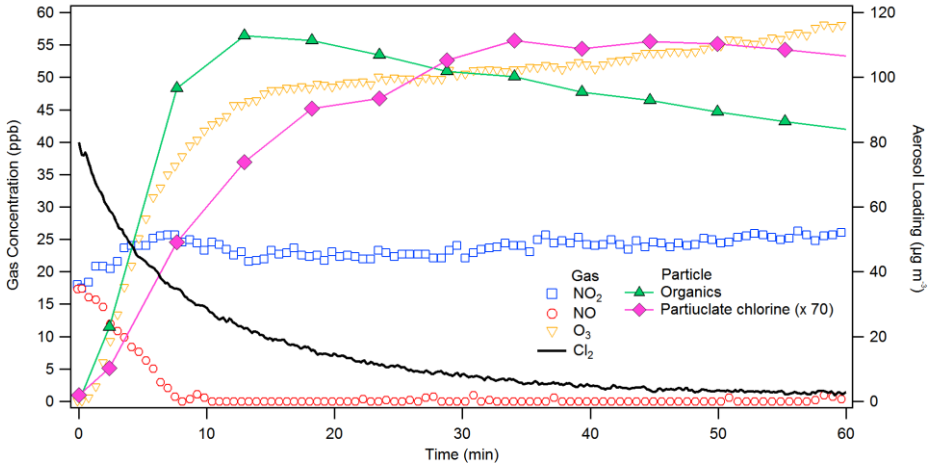

Figure 1: Representative trends of SOA and trace gas species during the photooxidation period. Data from dodecane oxidation (Exp. 11) are shown. Particulate chlorine concentrations were multiplied by 70 for ease of comparison.

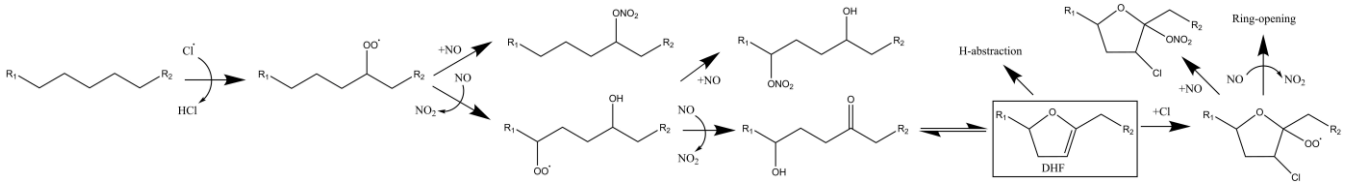

Figure 2: Formation pathway for chlorinated organics via chlorine addition to the DHF. H-abstraction from DHF is also possible. Ozone may also react with the double-bond on the DHF, competing with chlorine radicals.

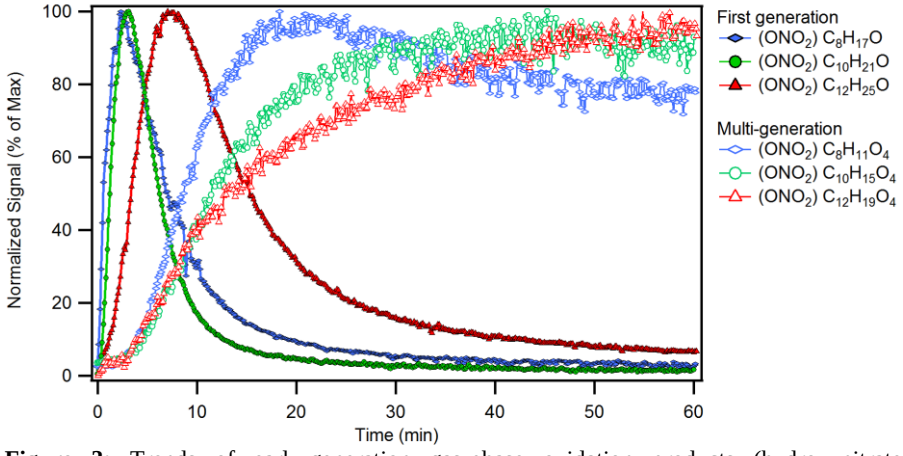

Figure 3: Trends of early-generation gas-phase oxidation products (hydroxynitrates) and multigeneration-oxidation products (hydroxycarbonyl nitrates) observed during chlorine-initiated oxidation of octane (Exp. 3), decane (Exp.7), and dodecane (Exp. 11). Species shown were first normalized against the I^- reagent ion signal and then normalized against their respective maxima.

Atmos. Chem. Phys. Discuss., https://doi.org/10.5194/acp-2018-443
Manuscript under review for journal Atmos. Chem. Phys.
Discussion started: 15 May 2018

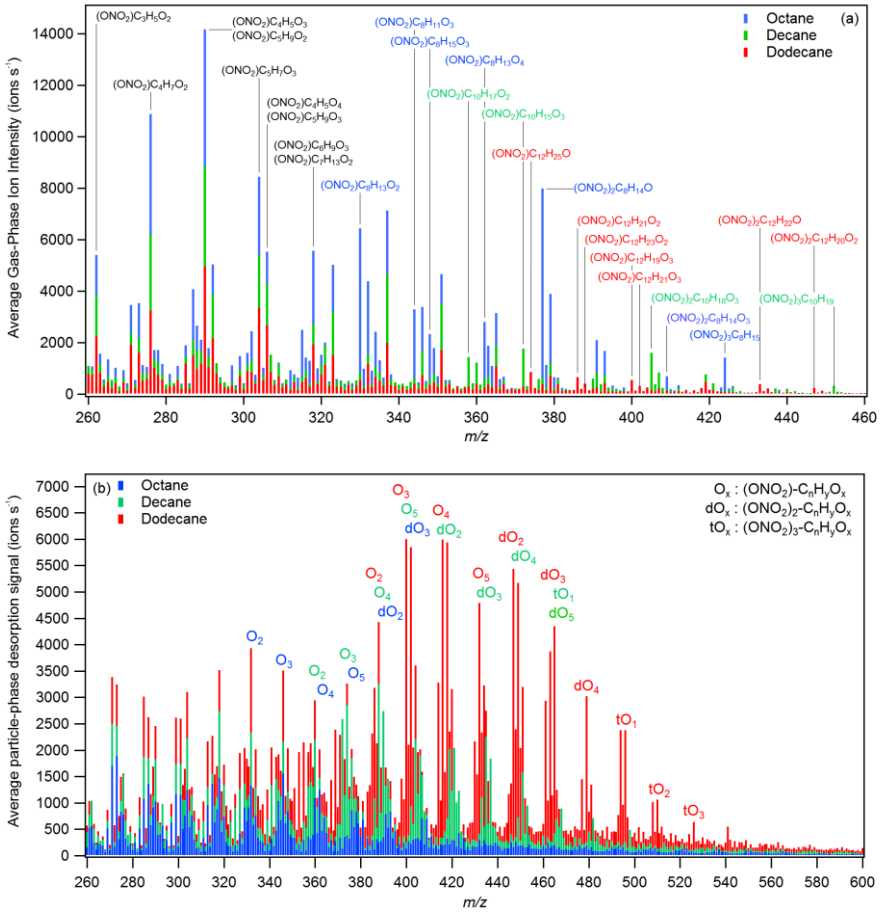

Figure 4: Comparison of (a) average gas-phase composition during the oxidation period and (b) particle-phase composition during FIGAERO desorption for octane (Exp. 3), decane (Exp. 7), and dodecane (Exp. 11). Color-coded ions indicate products that were much more abundant in reaction products derived from a particulate alkane precursor. In (b), O_x, dO_x, and tO_x were used as shorthand notations for oxidized organic nitrate, dinitrate, and trinitrates with x number of oxygens (excluding those from ONO_2). Sticks were not stacked, and no x-axis offset was applied during plotting.

Atmos. Chem. Phys. Discuss., https://doi.org/10.5194/acp-2018-443
Manuscript under review for journal Atmos. Chem. Phys.
Discussion started: 15 May 2018

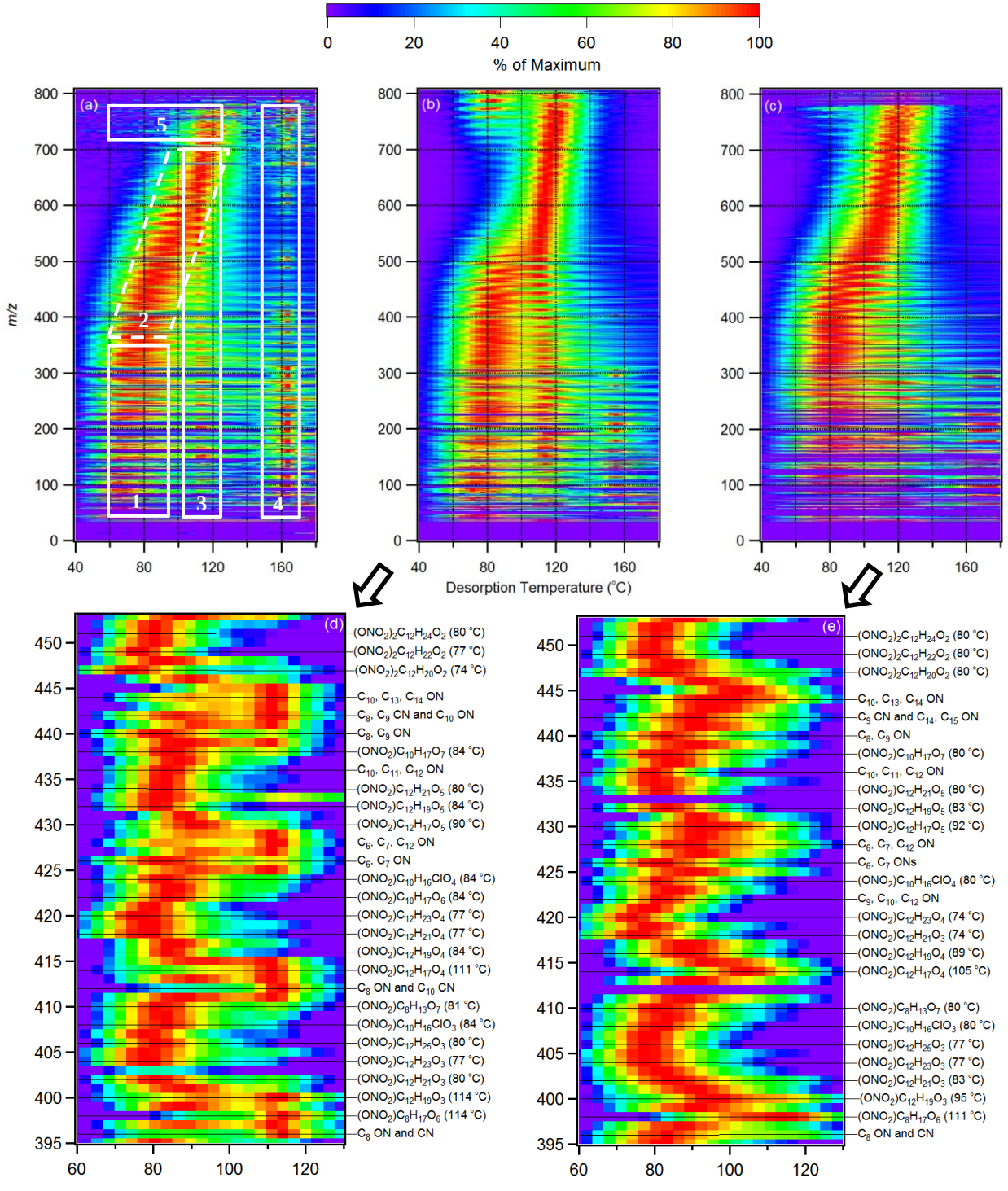

Figure 5: Comparison of two-dimensional thermograms for (a) octane-Cl SOA under low RH from Exp. 3, (b) dodecane-Cl SOA under low RH from Exp. 11, and (c) dodecane-Cl SOA under high RH (67 %) from Exp. 12. The color represents the ion intensity at a *m/z* as a percentage of the maximum desorption signal observed at that *m/z*. Different thermal desorption regions in (a) are dominated by (1) thermal

fragmentation products (2) monomers (3) oligomers and their decomposition products and (4) thermal decomposition of ammonium sulfate or extremely low volatility compounds. Region (5) is unresolved but appears to be thermally unstable oligomers. Region (2) and (3) can overlap, as shown in (d) for (b) and as shown in (e) for (c). At each nominal *m/z*, only the dominant ion is labeled in (d) and (e). If multiple ions of similar intensity were present, only general descriptions are given in the annotations, where "ON" stands for organonitrate and "CN" stands for chloronitrate. Non-nitrated organic ions were observed but not labeled because they were positioned in-between more intense organonitrates at neighboring *m/z* coordinates. T_{max} values are included in parenthesis. Increasing the RH suppressed oligomer formation, enhancing the monomer features in (c) and (e) when compared with (b) and (d). The *m/z* values shown includes the chemical ionization reagent I^- (*m/z* 127).

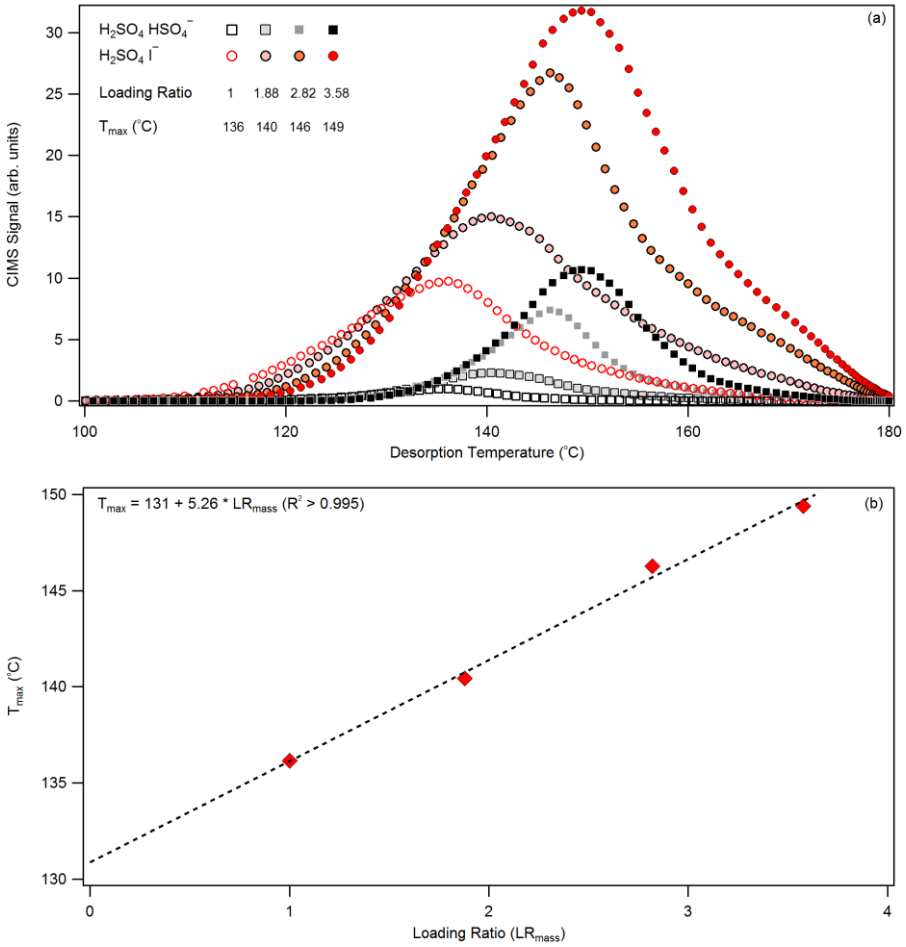

Figure 6: (a) The 1-D thermograms for two $(NH_4)_2SO_4$ decomposition product ions. $H_2SO_4 \bullet I^-$ was the primary adduct and $H_2SO_4 \bullet HSO_4^-$ was a secondary ionization product. The lowest time-integrated desorption ion intensity for $H_2SO_4\ I^-$ was used as the basis for calculating the loading ratio (LR_{mass}). The loading ratio for $H_2SO_4 \bullet HSO_4^-$ (not shown) is the square of that for $H_2SO_4\ I^-$ (b) Linear regression fitting of T_{max} as a function of the LR_{mass}